

Analysis of subwavelength metal hole array structure for the enhancement of back-illuminated quantum dot infrared photodetectors

Zahyun Ku,^{1,5} Woo-Yong Jang,^{2,5,6} Jiangfeng Zhou,^{3,5} Jun Oh Kim,² Ajit V. Barve,² Sinhara Silva,³ Sanjay Krishna,² S. R. J. Brueck,² Robert Nelson,¹ Augustine Urbas,¹ Sangwoo Kang,⁴ and Sang Jun Lee^{4,*}

¹Air Force Research Laboratory, Wright-Patterson Air Force Base, Ohio 45433, USA

²Center for High Technology Materials, Electrical and Computer Engineering Department, University of New Mexico, Albuquerque, New Mexico 87106, USA

³Department of Physics, University of South Florida, Tampa, Florida 33620, USA

⁴Division of Industrial Metrology, Korea Research Institute of Standards and Science, Daejeon 305-340, South Korea

⁵These authors contributed equally

⁶Currently with Air Force Research Laboratory, Wright-Patterson Air Force Base, Ohio 45433 USA

*sjlee@kriss.re.kr

Abstract: This paper is focused on analyzing the impact of a two-dimensional metal hole array structure integrated to the back-illuminated quantum dots-in-a-well (DWELL) infrared photodetectors. The metal hole array consisting of subwavelength-circular holes penetrating gold layer (2D-Au-CHA) provides the enhanced responsivity of DWELL infrared photodetector at certain wavelengths. The performance of 2D-Au-CHA is investigated by calculating the absorption of active layer in the DWELL structure using a finite integration technique. Simulation results show that the performance of the DWELL focal plane array (FPA) is improved by enhancing the coupling to active layer via local field engineering resulting from a surface plasmon polariton mode and a guided Fabry-Perot mode. Simulation method accomplished in this paper provides a generalized approach to optimize the design of any type of couplers integrated to infrared photodetectors. Experimental results demonstrate the enhanced signal-to-noise ratio by the 2D-Au-CHA integrated FPA as compared to the DWELL FPA. A comparison between the experiment and the simulation shows a good agreement.

©2013 Optical Society of America

OCIS codes: (050.6624) Subwavelength structures; (050.2230) Fabry-Perot; (130.2790) Guided waves; (230.5160) Photodetectors; (230.5750) Resonators; (240.6680) Surface plasmons.

References and links

1. V. Ryzhii, "The theory of quantum-dot infrared phototransistors," *Semicond. Sci. Technol.* **11**(5), 759–765 (1996).
2. S. Krishna, S. D. Gunapala, S. V. Bandara, C. Hill, and D. Z. Ting, "Quantum Dot Based Infrared Focal Plane Arrays," *Proc. IEEE* **95**(9), 1838–1852 (2007).
3. P. Boucaud and S. Sauvage, "Infrared photodetection with semiconductor self-assembled quantum dots," *C. R. Phys.* **4**(10), 1133–1154 (2003).
4. G. T. Liu, A. Stintz, H. Li, T. C. Newell, G. L. Gray, P. M. Varangis, K. J. Malloy, and L. F. Lester, "The Influence of Quantum-Well Composition on the Performance of Quantum Dot Lasers Using InAs/InGaAs Dots-in-a-Well (DWELL) Structures," *IEEE J. Quantum Electron.* **36**(11), 1272–1279 (2000).
5. A. Rogalski, J. Antoszewski, and L. Faraone, "Third-generation infrared photodetector arrays," *J. Appl. Phys.* **105**(9), 091101 (2009).
6. C. Genet and T. W. Ebbesen, "Light in tiny holes," *Nature* **445**(7123), 39–46 (2007).
7. D. Wasserman, E. A. Shaner, and J. G. Cederberg, "Midinfrared doping-tunable extraordinary transmission from sub-wavelength Gratings," *Appl. Phys. Lett.* **90**(19), 191102 (2007).

Report Documentation Page				Form Approved OMB No. 0704-0188	
Public reporting burden for the collection of information is estimated to average 1 hour per response, including the time for reviewing instructions, searching existing data sources, gathering and maintaining the data needed, and completing and reviewing the collection of information. Send comments regarding this burden estimate or any other aspect of this collection of information, including suggestions for reducing this burden, to Washington Headquarters Services, Directorate for Information Operations and Reports, 1215 Jefferson Davis Highway, Suite 1204, Arlington VA 22202-4302. Respondents should be aware that notwithstanding any other provision of law, no person shall be subject to a penalty for failing to comply with a collection of information if it does not display a currently valid OMB control number.					
1. REPORT DATE 25 FEB 2013		2. REPORT TYPE		3. DATES COVERED 00-00-2013 to 00-00-2013	
4. TITLE AND SUBTITLE Analysis of subwavelength metal hole array structure for the enhancement of back illuminated photodetectors				5a. CONTRACT NUMBER	
				5b. GRANT NUMBER	
				5c. PROGRAM ELEMENT NUMBER	
6. AUTHOR(S)				5d. PROJECT NUMBER	
				5e. TASK NUMBER	
				5f. WORK UNIT NUMBER	
7. PERFORMING ORGANIZATION NAME(S) AND ADDRESS(ES) Air Force Research Laboratory, Wright-Patterson Air Force Base, OH, 45433				8. PERFORMING ORGANIZATION REPORT NUMBER	
9. SPONSORING/MONITORING AGENCY NAME(S) AND ADDRESS(ES)				10. SPONSOR/MONITOR'S ACRONYM(S)	
				11. SPONSOR/MONITOR'S REPORT NUMBER(S)	
12. DISTRIBUTION/AVAILABILITY STATEMENT Approved for public release; distribution unlimited					
13. SUPPLEMENTARY NOTES Optics Express, Vol. 21, No. 4, 25 February 2013					
14. ABSTRACT					
15. SUBJECT TERMS					
16. SECURITY CLASSIFICATION OF:			17. LIMITATION OF ABSTRACT Same as Report (SAR)	18. NUMBER OF PAGES 9	19a. NAME OF RESPONSIBLE PERSON
a. REPORT unclassified	b. ABSTRACT unclassified	c. THIS PAGE unclassified			

8. C.-C. Chang, Y. D. Sharma, Y.-S. Kim, J. A. Bur, R. V. Shenoi, S. Krishna, D. Huang, and S.-Y. Lin, "A Surface Plasmon Enhanced Infrared Photodetector Based on InAs Quantum Dots," *Nano Lett.* **10**(5), 1704–1709 (2010).
9. S. C. Lee, Y. D. Sharma, S. Krishna, and S. R. J. Brueck, "Leaky-mode effects in plasmonic-coupled quantum dot infrared photodetectors," *Appl. Phys. Lett.* **100**(1), 011110 (2012).
10. J. Rosenberg, R. V. Shenoi, T. E. Vandervelde, S. Krishna, and O. Painter, "A multispectral and polarization-selective surface-plasmon resonant midinfrared detector," *Appl. Phys. Lett.* **95**(16), 161101 (2009).
11. S. J. Lee, Z. Ku, A. Barve, J. Montoya, W.-Y. Jang, S. R. J. Brueck, M. Sundaram, A. Reisinger, S. Krishna, and S. K. Noh, "A monolithically integrated plasmonic infrared quantum dot camera," *Nat. Commun.* **2**, 286 (2011).
12. www.cst.com
13. M. G. Moharam and T. K. Gaylord, "Rigorous coupled-wave analysis of planar-grating diffraction," *J. Opt. Soc. Am.* **71**(7), 811–818 (1981).
14. I. N. Stranski and L. Krastanow, "Sitzungsberichte d. Akad. D. Wissenschaften in Wien," *Abt. IIb, Band 146*, 797–810 (1937).
15. D. Xia, Z. Ku, S. C. Lee, and S. R. J. Brueck, "Nanostructures and Functional Materials Fabricated by Interferometric Lithography," *Adv. Mater. (Deerfield Beach Fla.)* **23**(2), 147–179 (2011).
16. M. A. Ordal, L. L. Long, R. J. Bell, S. E. Bell, R. R. Bell, R. W. Alexander, Jr., and C. A. Ward, "Optical properties of the metals Al, Co, Cu, Au, Fe, Pb, Ni, Pd, Pt, Ag, Ti, and W in the infrared and far infrared," *Appl. Opt.* **22**(7), 1099–20 (1983).
17. I. Brenner, (personal communication).
18. W. G. Spitzer and J. M. Whelan, "Infrared Absorption and Electron Effective Mass in n-Type Gallium Arsenide," *Phys. Rev.* **114**(1), 59–63 (1959).
19. A. Barve, T. Rotter, Y. Sharma, S. J. Lee, S. K. Noh, and S. Krishna, "Systematic study of different transitions in high operating temperature quantum dots in a well photodetectors," *Appl. Phys. Lett.* **97**(6), 061105 (2010).
20. J. D. Jackson, *Classical Electrodynamics* (Wiley, New York, 3rd Edition, 1999).
21. I. O. Kim, S. Sengupta, A. V. Barve, Y. D. Sharma, S. Adhikary, S. J. Lee, S. K. Noh, M. S. Allen, J. W. Allen, S. Chakrabarti, and S. Krishna, "Multi-stack InAs/InGaAs Sub-monolayer Quantum Dots Infrared Photodetectors," *Appl. Phys. Lett.* **102**(1), 011131 (2013).
22. E. L. Dereniak and G. Boreman, *Infrared Detectors and Systems* (Wiley, 1996).
23. T. E. Vandervelde, M. C. Lenz, E. Varley, A. Barve, J. Shao, R. Shenoi, D. A. Ramirez, W.-Y. Jang, Y. D. Sharma, and S. Krishna, "Quantum Dots-in-a-Well Focal Plane Arrays," *IEEE J. Sel. Top. Quantum Electron.* **14**(4), 1150–1161 (2008).
24. J. R. Andrews, S. R. Restaino, S. W. Teare, Y. D. Sharma, W.-Y. Jang, T. E. Vandervelde, J. S. Brown, A. Reisinger, M. Sundaram, S. Krishna, and L. Lester, "Comparison of Quantum Dots-in-a-Double-Well and Quantum Dots-in-a-Well Focal Plane Arrays in the Long-Wave Infrared," *IEEE Trans. Electron. Dev.* **58**(7), 2022–2027 (2011).

1. Introduction

In the past decade, the infrared detectors based on intersubband transitions in quantum dots (QDs) have attracted much attention due to lower dark currents and increased lifetimes compared with quantum well infrared photodetectors, which are in turn due to three-dimensional confinement and the reduction of scattering, respectively [1,2]. These epitaxially self-assembled and nanometer-scale QD islands form spontaneously on a semiconductor substrate because of lattice mismatch [3]. More recently, infrared detectors based on QDs embedded in a quantum well (QW), known as dots-in-a-well (DWELL) heterostructure, have been proposed [4]. The DWELL architecture brings the advantages of QWs, such as control over the operating wavelength, while maintaining the advantages of QDs, such as normal incidence operation [5]. In parallel, focal plane array (FPA) development for infrared imaging has proceeded from the first to third generations (linear arrays, 2D arrays for staring systems, and large format with enhanced capabilities, respectively). For a step closer to the next generation of FPAs, we envision that perforated metal film structures [6,7] will improve the performance of FPA by enhancing the coupling to photodetectors via local field engineering, and will enable spectral sensitivity modifications. In regard to the improved performance at certain wavelengths, it is worth pointing out the structural difference between previous perforated metal film integrated front-illuminated single pixel devices [8–10] and our back-illuminated device (FPA) [11]. Apart from the pixel linear dimension, it is a distinct difference that there is a metal cladding (composed of a number of metals for ohmic contact and the read-out integrated circuit hybridization) in the FPA between the heavily doped gallium arsenide (GaAs) used as the contact layer and the read-out integrated circuit (i.e., n-type GaAs/QD-absorber/n-type GaAs/metal cladding/ROIC); on the contrary, the front-illuminated single pixel device consists of two heavily doped contact layers separated by the

QD-absorber on a semi-infinite GaAs substrate (i.e., n-type GaAs/QD-absorber/n-type GaAs/substrate).

In this paper, a single metal layer is chosen as the metal cladding in the simulation to allow clearer demonstration of the effects of a two-dimensional square array of circular holes in Au layer (2D-Au-CHA). As a result of the 2D-Au-CHA and metal ground plane, the 2D-Au-CHA integrated DWELL FPA (2D-Au-CHA:DWELL FPA) yields a wavelength selective resonant enhancement of the detector response in the mid-infrared spectral region. The analysis and comparison of modeling results with experiment indicates a good quantitative agreement of the improved performance of DWELL FPA measured using the signal to noise (SNR) and the noise equivalent difference in temperature (NEDT) at resonance wavelengths. The improved performance results from a surface plasmon polariton (SPP) mode and a guided Fabry-Perot mode, that enhance x or y (along the polarization direction used in simulation) and z (along the growth direction) components of electric field in the active region compared with the unmodified DWELL FPA at certain wavelengths.

2. Structure of 2D-Au-CHA integrated DWELL based back-illuminated infrared photodetector

In order to find the optimum dimension of 2D-Au-CHA to match the first order SPP resonance with the maximum of DWELL FPA's spectral response, we employed both the commercial software (CST Microwave Studio: Computer Simulation Technology GmbH, Darmstadt, Germany) [12] based on a finite integration technique and a rigorous coupled wave analysis [13]. Comparable results were obtained for both techniques (not shown here).

Indium arsenide (InAs) QDs were grown with VG-80 solid source molecular beam epitaxy (MBE) system using a Stranski–Krastanow growth mode [14]. After the MBE growth, the FPA was fabricated (a dry etch to form the mesa, surface passivation (SiNx), ohmic metal evaporation, under bump metallization, indium deposition, and indium reflow process) and then hybridized to the read-out integrated circuit by flip-chip bonding processing. Following the removal of substrate and AlAs etch stop layer, the 2D-Au-CHA was fabricated on a 1 μm thick contact layer of the DWELL FPA as shown in Fig. 1(a). The schematic diagram in Fig. 1(a) illustrates a pixel in the 2D-Au-CHA:DWELL FPA. The zoomed-in image in Fig. 1(b) depicts the DWELL heterostructure within a pixel. The DWELL structure includes the n-doped GaAs contact layers with 200/1000 nm thicknesses, the active region with 20 stacks of InAs QDs embedded in 3.5 nm thick $\text{In}_{0.15}\text{Ga}_{0.85}\text{As}/\text{Al}_{0.08}\text{Ga}_{0.92}\text{As}$ QWs, each separated by 50 nm thick $\text{Al}_{0.08}\text{Ga}_{0.92}\text{As}$ barriers. Figure 1(c) shows geometrical parameters of a simplified unit cell of the 2D-Au-CHA:DWELL FPA used in the simulation. The details of MBE growth/fabrication of DWELL FPA and 2D-Au-CHA are available in Ref [11,15].

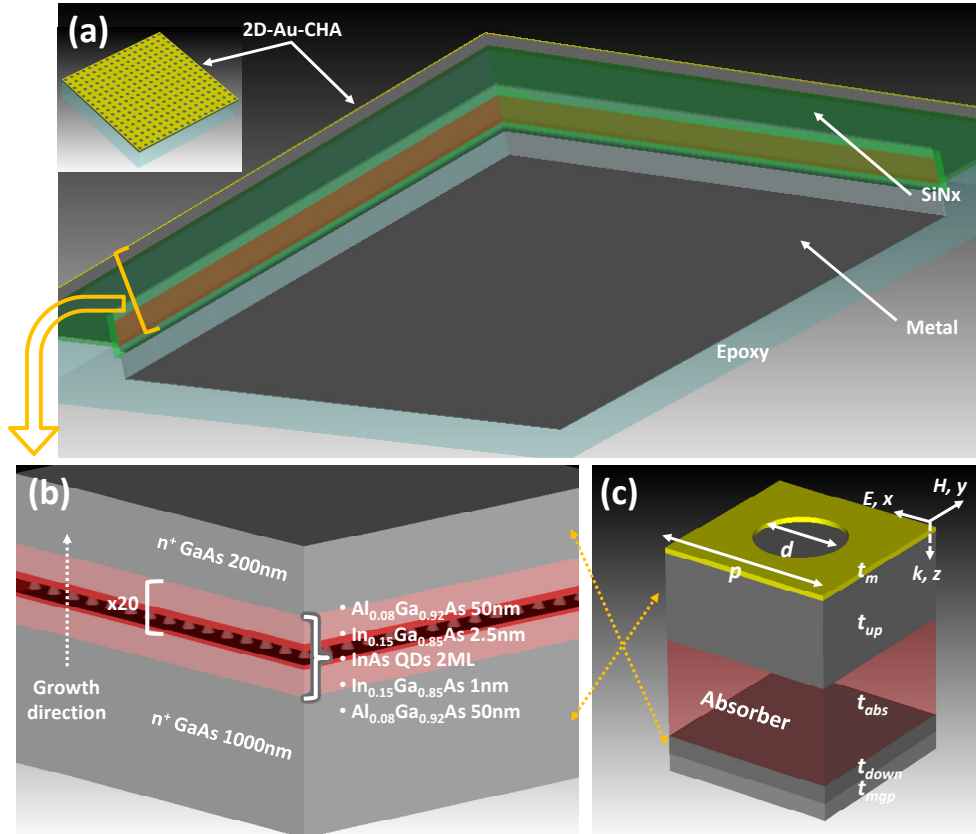


Fig. 1. Illustration of (a) a pixel in the 2D-Au-CHA:DWELL FPA (after substrate and AlAs etch stop layer were removed) and (b) the DWELL heterostructure. (c) Schematic view of a simplified unit cell of the 2D-Au-CHA:DWELL FPA used for numerical simulation. Geometrical parameters of 2D-Au-CHA:DWELL FPA: $p = 1.8 \mu\text{m}$; $d = p/2$; $t_m = 50 \text{ nm}$; $t_{up} = 1 \mu\text{m}$; $t_{abs} = 1.12 \mu\text{m}$; $t_{down} = 0.2 \mu\text{m}$; $t_{mgp} = 0.2 \mu\text{m}$. In addition, the configuration of polarization and propagation is depicted (E , H , and k denote electric field, magnetic field, and wave vector, respectively).

3. Simulated absorption, responsivity and enhancement ratio

For the purpose of understanding our experimental results quantitatively and qualitatively, we performed 3D full field electromagnetic simulations of 2D-Au-CHA:DWELL FPA using a finite integration technique. The boundary conditions on the faces (of a single cubic unit cell) parallel to the propagation vector were set as perfect magnetic/electric conductor to approximate a TEM plane wave propagating through 2D-Au-CHA:DWELL FPA as shown in Fig. 1(c). All geometrical parameters are indicated in Fig. 1(c). For materials constituting 2D-Au-CHA:DWELL FPA, a Drude model was applied for the dielectric parameters of Au [16] (1.4 times larger scattering frequency than bulk Au to fit the experimental values obtained from Sandia National Laboratory [17]), n-type GaAs [9,18] ($2 \times 10^{18} \text{ cm}^{-3}$) and lossy aluminium [16] used as 2D-Au-CHA, contact layer and metal ground plane, respectively. Figures 1(b) and 1(c) show that 20 stacks of QD layers were simplified to an effective absorber layer whose n_{eff} and k_{eff} (real and imaginary parts of refractive index in effective absorber) were taken from Ref [9], measured quantum efficiency [19], and spectral photoresponse.

The absorption in the active layer (or effective absorber) is only useful to determine how much the response (e.g., photocurrent, responsivity, or SNR) is enhanced with 2D-Au-CHA, i.e., the absorption of other layers is parasitic. The power absorbed per unit volume can be

calculated from the divergence of the Poynting vector ($\nabla \cdot \vec{S}$) and is equivalent to $\frac{\omega \epsilon''(\lambda) |E(\lambda)|^2}{2}$, where ω is the angular frequency ($2\pi c/\lambda$), c is the speed of light in vacuum, $\epsilon''(\lambda)$ is the imaginary part of dielectric permittivity, and $|E(\lambda)|^2$ is the intensity of the electric field [20]. Therefore, the absorption in one of the layers constituting 2D-Au-CHA:DWELL FPA is calculated by $\int \frac{\omega \epsilon''_i(\lambda) |E_i(\lambda)|^2}{2} dV_i$, where i = 2D-Au-CHA, contact layers, effective absorber or metal ground plane. However, the absorption in effective absorber should be calculated carefully because the QD based infrared photodetector shows different response [3] depending on the orientation of electric field intensity ($|E_x|^2$, $|E_y|^2$, or $|E_z|^2$). More specifically, the effective absorber's absorption due to 2D-Au-CHA is

$$A_{EA}^{2D-Au-CHA} = \int \frac{\omega \epsilon''_{EA}(\lambda) \cdot \left[|E_{EA}^x(\lambda)|^2 + \eta |E_{EA}^z(\lambda)|^2 \right]}{2} dV_{EA} \quad (1)$$

where, $|E_{EA}^j|^2$ is the intensity of j component-electric field in the effective absorber and ~ 8 is used for η (electric field along the growth direction shown in Fig. 1(b) is dominant in interacting with the QDs as compared to the electric field parallel to the perforated metal film) [21]. Figure 2 shows the calculated absorption in each layer of the considered 2D-Au-CHA:DWELL FPA (calculated absorption of DWELL FPA is not shown here).

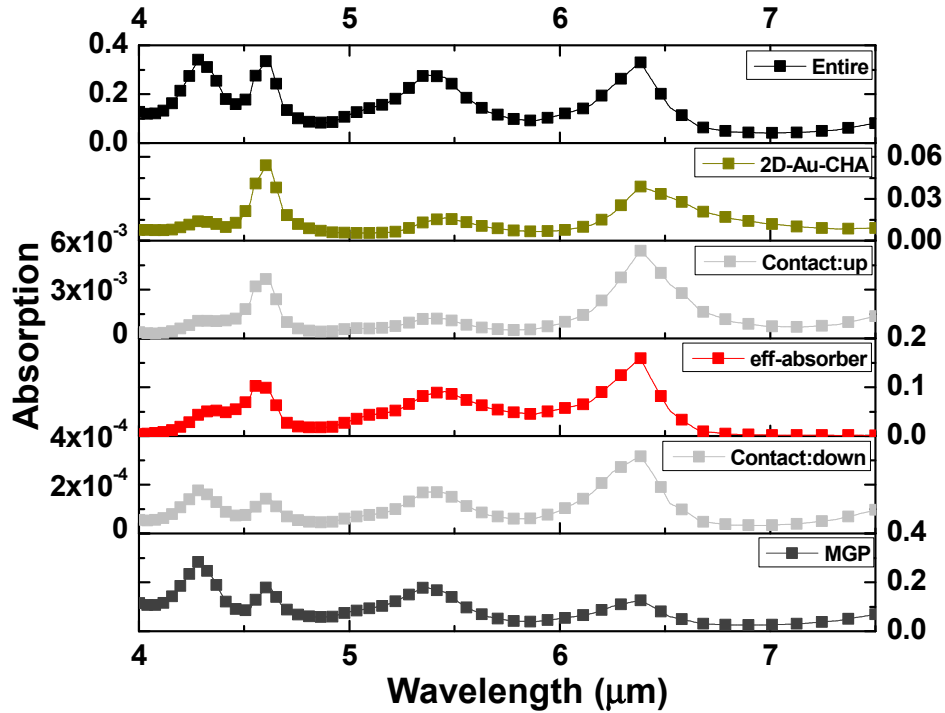


Fig. 2. Absorption calculated in the different layers of the 2D-Au-CHA:DWELL FPA as a function of the illumination wavelength.

Both DWELL FPA and 2D-Au-CHA:DWELL FPA are illuminated under the blackbody at 423 K (the temperature used for measurements [11]). Using the absorption in the effective absorber as shown in Fig. 2, we calculate the responsivity (R), $R_k(\lambda) = A_{EA}^k \cdot R_{BB \text{ at } 423K}$, where

k is 2D-Au-CHA:DWELL FPA (or DWELL FPA), R_{BB} at 423K can be evaluated using Planck's law for the blackbody at 423 K and the equivalent spectral current density, $J(\lambda) = N_0(\lambda) \times e^-$. $N_0(\lambda)$ is the incident photon flux and e^- is the electron charge. Here, it is assumed that an electron-hole pair is collected for each photon absorbed in effective absorber, which corresponds to an internal quantum efficiency equal to 1. Figure 3 shows the simulated responsivities of DWELL FPA and 2D-Au-CHA:DWELL FPA. Moreover, in order to estimate the influence of the 2D-Au-CHA on the enhancement of the DWELL FPA efficiency, we illustrate in Fig. 3 the ratio between the responsivity of 2D-Au-CHA:DWELL FPA over the responsivity of DWELL FPA, which is represented by the red circle and agrees well with the SNR measurements as will be shown in Fig. 4. Clearly there are resonances at $\sim 4.56 \mu\text{m}$, $\sim 5.45 \mu\text{m}$, and $\sim 6.38 \mu\text{m}$. It is of great importance to investigate the electric field distributions in the effective absorber at resonant wavelengths because the absorption is related to the orientation and intensity of electric fields as shown in Eq. (1) and the effective absorber is especially sensitive to E_z due to η . In addition, understanding this mechanism helps us to improve the design of the perforated metal film integrated infrared FPA. At $4.56 \mu\text{m}$ and $6.38 \mu\text{m}$, E_x distribution in z direction is not due to the propagating modes shown in perforated metal film integrated front-illuminated device, but rather to the guided Fabry-Perot modes resulting from the presence of metal ground plane in the FPA structure; E_z distribution in the plane parallel to the perforated metal film exhibits the SPP modes (1st and 2nd order SPPs owing to the interaction between the first and second nearest apertures, respectively); E_z in z direction displays the exponential decay of a surface wave as shown in the insets of Fig. 3. The responsivity at $5.45 \mu\text{m}$ is increased by the guided Fabry-Perot mode, evidenced by a standing wave pattern of E_x along z direction depicted in the inset of Fig. 3.

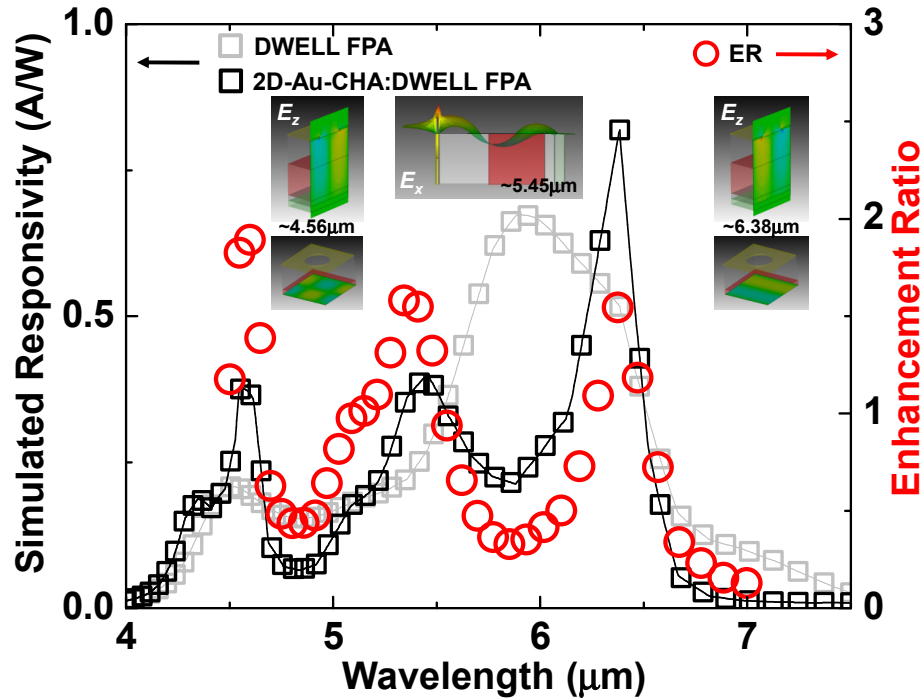


Fig. 3. Simulated responsivities of the DWELL FPA (gray square), 2D-Au-CHA:DWELL FPA (black square) and enhancement ratio (red circle) resulting from 2D-Au-CHA, i.e., $R_{2D-Au-CHA:DWELL FPA} / R_{DWELL FPA}$. Note that unity internal quantum efficiency in effective absorbing layer is used. The simulated electric field distributions at the corresponding resonances (resulting from surface plasmon polariton and guided Fabry-Perot modes) are shown in the inset to the figure.

4. Signal to noise and noise equivalent difference in temperature

To accurately quantify the resonant enhancement, we consider the SNRs of 2D-Au-CHA:DWELL FPA and DWELL FPA. The signal is the intensity of averaged spectral response and the noise is the standard deviation of spectral response over 20 frames. Subsequently, the SNRs of 2D-Au-CHA:DWELL FPA and DWELL FPA were computed and shown in Fig. 4 for the entire wavelength range. By taking the ratio between the SNRs of 2D-Au-CHA:DWELL FPA and DWELL FPA, we extracted three enhancement ratios, 1.63 (4.5 μm), 1.21 (5.5 μm), and 1.59 (6.1 μm) by 2D-Au-CHA:DWELL FPA, respectively. The overall agreement between experimental results and the simulated enhancement ratios at the corresponding resonance is apparent from Fig. 3. Error in resonance wavelengths between simulation and experiment, $\Delta\lambda = (\lambda_{sim} - \lambda_{exp})/\lambda_{exp}$, is less than 5%, which can be attributed to imperfections and variation from the fabrication process. The enhancement ratios over the full spectrum are shown in Fig. 4.

In addition, the NEDT for 2D-Au-CHA:DWELL FPA at a device temperature of 77 K was measured by changing the irradiance via a calibrated blackbody source at various scene temperatures. By definition, the NEDT (in units of mK) is a performance measure of FPA's sensitivity which indicates the smallest uniform scene temperature difference the FPA can detect. In the measurement setup, we used a narrowband optical filter centered at 5.95 μm with $\Delta\lambda \sim 140$ nm in front of the blackbody source for demonstrating the sensitivity enhancement near the first resonance. NEDT values were obtained by using the FPA's output response (ΔV_0) between two temperatures of the blackbody source (ΔT), along with the recorded noise (V_n) at the lower temperature with the following equation [22–24]: $\text{NEDT} = \Delta T / (\Delta V_0 / V_n)$. We computed the NEDT averaged over 121 uniform and well-behaved pixels on the array. The averaged NEDTs of 2D-Au-CHA:DWELL FPA and DWELL FPA were 77.3 mK and 109.1 mK at an irradiance of 3.65×10^{-5} W/cm². By comparison, this corresponds to a sensitivity improvement of 2D-Au-CHA:DWELL FPA by a factor of 1.4 times over DWELL FPA.

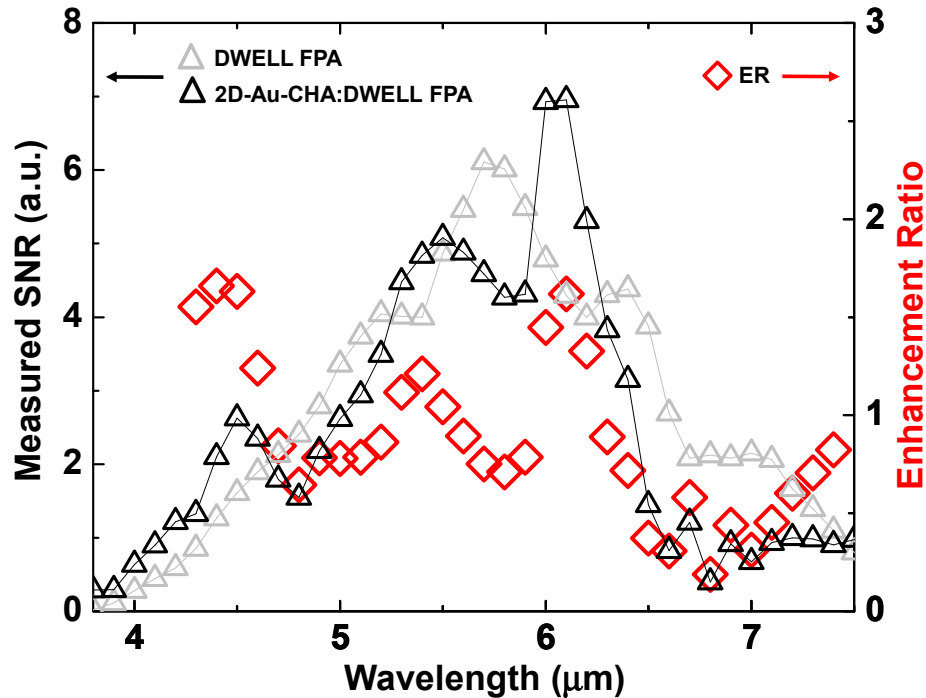


Fig. 4. Experimental SNRs of the DWELL FPA (gray triangle) and 2D-Au-CHA:DWELL FPA (black triangle), and the corresponding enhancement ratio (red diamond) by 2D-Au-CHA:DWELL FPA over the DWELL FPA.

5. Conclusion

In summary, we have investigated the effect of 2D-Au-CHA on the performance of an infrared DWELL FPA both numerically and experimentally. The wavelength selective enhancement due to the 2D-Au-CHA (or perforated metal film) in an infrared FPA could have a dramatic impact on multispectral (or hyperspectral) imaging system construction. Understanding the underlying mechanism by means of a simulation may offer the possibility to explore a large variety of phenomena in the next generation of infrared detectors associated with surface plasmon polariton and guided Fabry-Perot modes, as well as applications in polarimetric infrared imaging and the improvement of the design of infrared detectors integrated with any type of couplers. A useful result is that the enhanced electric fields inside the effective absorber are strongly associated with the thickness of contact layer and QD layer (i.e., spacer between perforated metal film and metal ground plane), therefore additional design and fabrication refinement are needed for better performance of the perforated metal film integrated FPA.

Acknowledgments

This work was supported by the Korea Research Institute of Standards and Science under the project “Study of infrared surface plasmon resonance for optical enhancement and wavelength tuning”, grant JP2012-0001. We also acknowledge AFRL contract FA9453-12-1-0131.